

Anisotropy of the Yellowstone Hot Spot Wake, Eastern Snake River Plain, Idaho

DEREK SCHUTT,¹ EUGENE D. HUMPHREYS¹ and KEN DUEKER²

Abstract—Over the last 10 million years, the Yellowstone hot spot has passed beneath the eastern Snake River Plain, both magmatically modifying the Snake River Plain crust and creating a wider, wake-like “tectonic parabola” of seismicity and uplift. Analysis of SKS arrivals to a line array of 55 mostly broadband stations, distributed across the tectonic parabola, reveals a nearly uniform orientation of anisotropy, with an average fast axis orientation of N64E. The back azimuth of null splitting events is parallel to the measured fast axis, suggesting that anisotropic material consists of a single layer. Splitting parameters are independent of backazimuth, suggesting that anisotropy is constant beneath each station. Thus station-averaged split parameters are representative of the anisotropy beneath the station. Station-averaged split times range from 0.6–1.5 s, and define a pronounced depression in split times centered about 80 km southeast of the axis of the Snake River Plain.

Assuming the degree of anisotropy (averaged over the ray path) to be no more than 10%, the split times are far too great for the anisotropy to be confined solely to the lithosphere. The simplest way to explain the observed anisotropy structure is to attribute it to simple shear strain caused by the absolute motion of North America. Because anisotropy is different in nearby Colorado and Nevada, we hypothesize that fossil anisotropy created in past orogens and continent-building events in the Snake River Plain area has been reset or erased by the passage of the hot spot, and that subsequent strain of the hot spot-related asthenospheric wake created a uniformly oriented fast axis. If this is true, then our array constrains the minimum of the hot spot’s asthenospheric wake.

Key words: Shear wave splitting, hot spot, mantle plume, anisotropy, yellowstone, shear wave anisotropy, SKS splitting.

Introduction

Several observations suggest the hot spot currently exciting Yellowstone magmatism has passed beneath the eastern Snake River Plain (eSRP) of southern Idaho. These include: 1) a series of time progressive rhyolitic calderas younging from the southwest to the northeast (SMITH and BRAILE, 1994); 2) a seismically inferred mid-crustal basaltic sill beneath the rhyolitic calderas (SPARLIN *et al.*, 1982); 3) a geoid high centered on Yellowstone that is thought to be caused by a deep low density anomaly (MILBERT, 1991); 4) He³/He⁴ values indicative of

¹Department of Geological Sciences, 1272 University of Oregon; Eugene, OR 97403-1272, U.S.A.
e-mail: schuttd@newberry.uoregon.edu.

²CIRES, University of Colorado at Boulder, Boulder, CO 80309-0449, U.S.A.

degassing primitive mantle (HEARN *et al.*, 1990); and 5) a parabolic-shaped region of heightened elevation, seismicity, and faulting, which is thought to have formed as hot spot mantle buoyantly flattened beneath North America (ANDERS and SLEEP, 1992; PIERCE and MORGAN, 1992; RIBE and CHRISTENSEN; SMITH and BRAILE, 1994).

To address the mantle structure and dynamics of this system, the Program for the Array Seismic Studies of the Continental Lithosphere (PASSCAL) supported the deployment of a 470 km long SW-trending line array of 55 mostly broadband stations across the width of the tectonic parabola in a line perpendicular to the path of the hot spot, crossing the eSRP at the location where the hot spot was active about 8 Ma (PIERCE and MORGAN, 1992; Fig. 1). These stations collected about 375 teleseismic events, which were used for an integrated *P* wave and *S* wave, and receiver function study of the upper mantle and crust in this area. Information about the mantle structure below this region can provide clues to understanding the mechanisms driving the hot spot, as well as giving insight into how variations in the physical state of the mantle have created the topography in the eSRP. This paper will be concentrated on the *S*-wave splitting component of our studies, which may be especially useful in providing information on the strain evolution of this hot spot asthenosphere.

Shear-wave Splitting Results

Data and Method

Over the 200-day life of the experiment, 59 shear-wave events were recorded. Of these, 32 had significant radial SKS energy that was not polluted by other phases. A record section of one of these SKS events is shown in Figure 2. In this case SKS phase is the first arriving, although we also measured splits on events where this was not the case.

We measured 141 sets of SKS split parameters. In addition, 30 events came in from backazimuths that produced no *SH* energy. These “null splitting” events occur when the ray travels along the fast or slow axes; these null events also constrain the orientation of the axes, although they do not provide any information on the split time.

We estimate anisotropy beneath our array by applying the tangential energy minimization technique of SILVER and CHAN (1991) to SKS arrivals. This method determines splitting parameters (split time and the horizontal projection of fast axis orientation) for each split observation by seeking transverse energy minima (Fig. 3—Top). As is standard in this analysis, transverse anisotropy and hexagonal symmetry are assumed. We show below that these assumptions are reasonable.

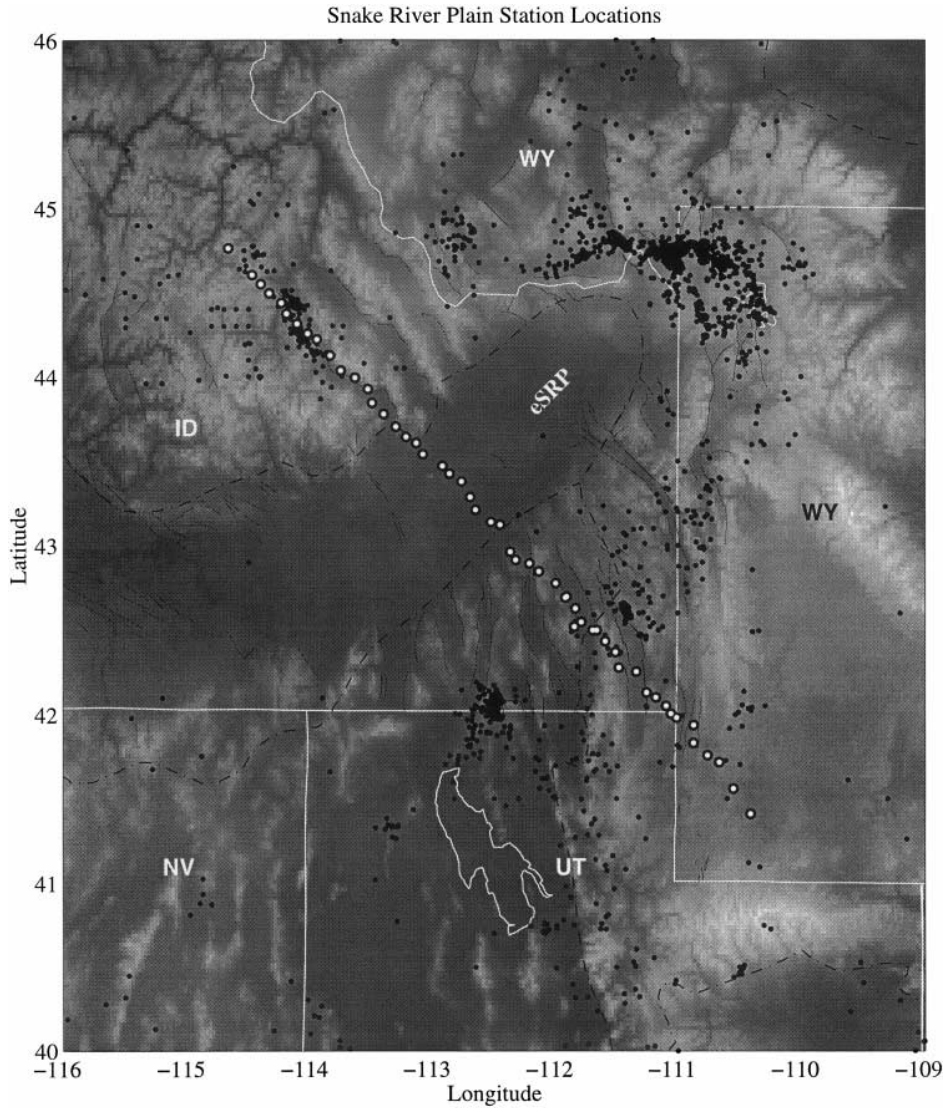


Figure 1

1993 Snake River Plain station locations. The array consisted of 55 mostly broadband seismometers stationed along a line 470 km long that runs perpendicular to the axis of the eastern Snake River Plain (eSRP), crossing the track of the hot spot near the location where magmatism was active ~ 8 Ma. Earthquakes are shown with black dots, and elevation indicated with shading. The tectonic parabola is defined by the parabolic concentration of earthquakes surrounding the eSRP in a wake-like fashion, with Yellowstone lying in the seismically active NW corner of Wyoming (WY).

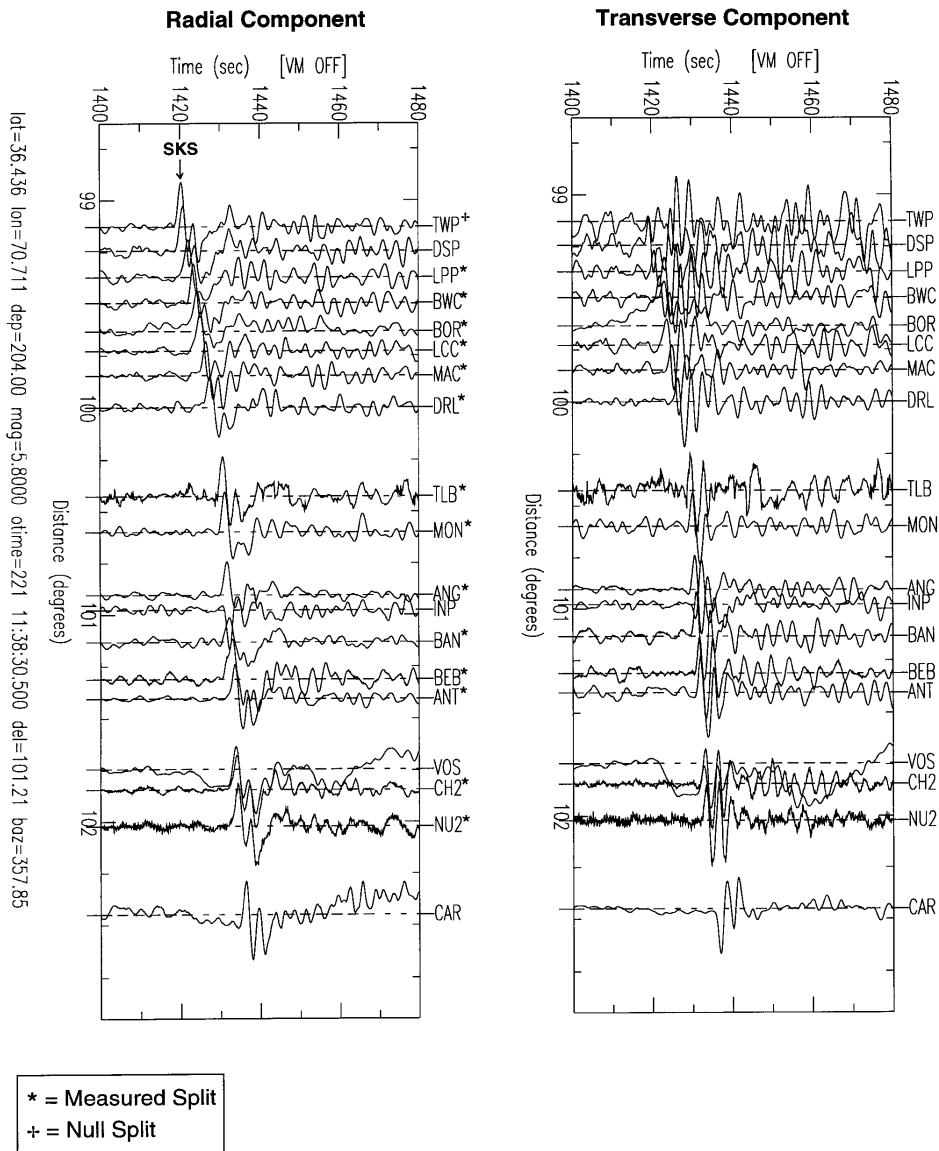


Figure 2

A record section from an average SKS event. This is certainly not the best event we received, but neither is it the worst of the 32 events with clear SKS energy. Traces are scaled individually, so that maximum amplitude displayed is the same from trace to trace. In general, for this event, the signal-to-noise ratio is lower for the transverse, by a factor of approximately 2–4. Good splits are those with split time errors of under 0.6 s. Although the single null split looks like it has energy on the transverse component, this particular trace is highly amplified. If one follows the moveout curve, there is no clear arrival at 1419 s, where one would expect to find the initial SKS energy. We also used the adjusted transverse energy plot for each station to help determine whether a split is null or not. If the transverse energy is minimum along the backazimuth of the arrival, this provides a good indication that the transverse energy seen is just noise. Of course the final determination is subjective, which motivated us to do the bulk statistical analysis which led to the station averages.

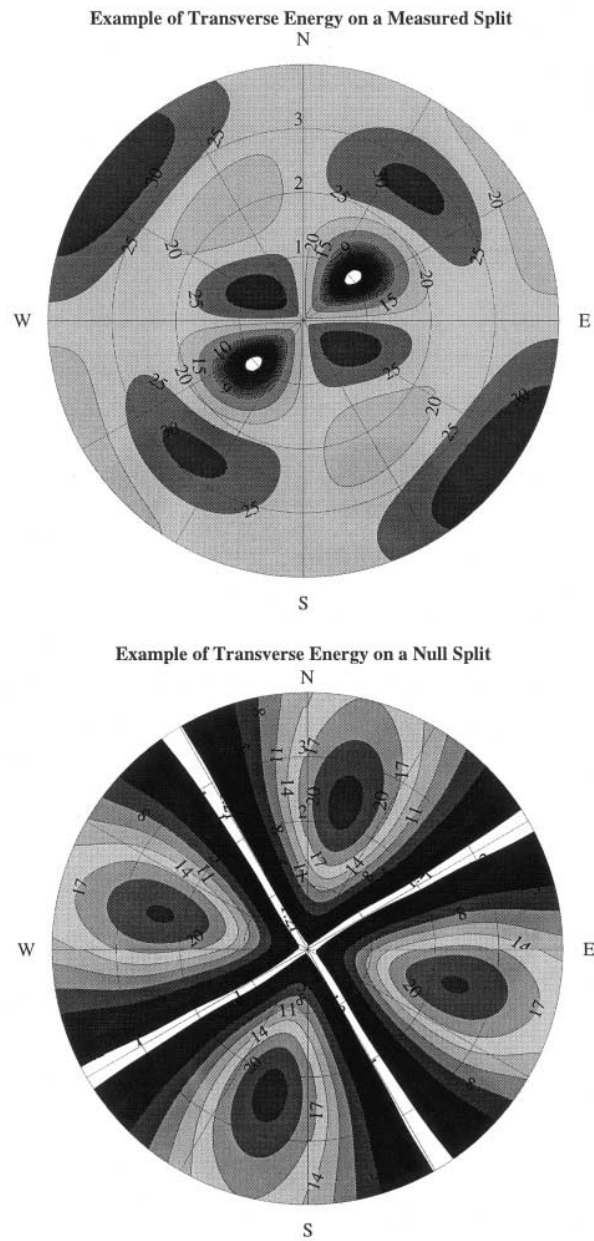


Figure 3

Plots of transverse energy as a function of fast axis orientation and split time. The minimum corrected energy gives the maximum likelihood split parameters. Radial distance is split time in seconds and angle is orientation of the fast axis. Energy levels are in relative units, normalized so that the 95% confidence bounds are indicated by the white area. (Top) Example for a split arrival. (Bottom) Example for a null split arrival.

Table 1
Raw SKS splitting data

Station	Lat. (°)	Long. (°)	ϕ (°)	ϕ_{err} (°)	δt (s)	δt_{err} (s)
CAV	41.7170	-110.6650	53	20	0	0
CAV	41.7170	-110.6650	62	16	0.70	0.20
NUG	41.8311	-110.8740	57	25	0	0
NU2	41.8319	-110.8740	50	10	1.15	0.25
LDC	41.9375	-110.8730	98	2	1.60	0.30
CH2*	42.0058	-111.0570	82	22	0.25	0.32
CH2	42.0058	-111.0570	34	8	1.05	0.12
CH2	42.0058	-111.0570	49	2	1.05	0.07
CH2	42.0058	-111.0570	41	2	1.85	0.25
DAH	42.0522	-111.0960	42	10	1.20	0.35
DAH	42.0522	-111.0960	67	9	0	0
VOS	42.1030	-111.1800	59	6	1.05	0.18
VOS	42.1030	-111.1800	66	9	0.90	0.10
VOS	42.1030	-111.1800	56	10	0.90	0.28
VOS	42.1030	-111.1800	70	30	0	0
MEM	42.1317	-111.2560	45	2	1.40	0.10
MEM	42.1317	-111.2560	65	11	0.65	0.12
AIR	42.2541	-111.3390	77	12	0.95	0.28
AIR	42.2541	-111.3390	58	18	1.25	0.50
MIC	42.2784	-111.4820	57	7	1.45	0.28
MIC	42.2784	-111.4820	49	5	1.05	0.13
MIC*	42.2784	-111.4820	123	2	2.30	0.23
MIC	42.2784	-111.4820	66	2	1.20	0.18
MIC	42.2784	-111.4820	44	5	1.30	0.30
MIC	42.2784	-111.4820	42	4	1.30	0.20
MIC	42.2784	-111.4820	41	8	0.80	0.15
MIC	42.2784	-111.4820	69	16	0	0
EMC	42.3694	-111.5090	41	6	1.30	0.30
EMC	42.3694	-111.5090	47	4	1.40	0.45
EMC	42.3694	-111.5090	47	7	1.40	0.30
EMC	42.3694	-111.5090	70	30	0	0
ANT	42.4340	-111.5930	63	4	1.30	0.40
ANT	42.4340	-111.5930	63	2	1.35	0.10
ANT	42.4340	-111.5930	69	8	1.20	0.38
ANT	42.4340	-111.5930	68	2	1.50	0.10
ANT	42.4340	-111.5930	68	11	1.15	0.25
ANT	42.4340	-111.5930	46	6	1.40	0.35
ANT	42.4340	-111.5930	55	8	1.10	0.20
ANT	42.4340	-111.5930	73	12	1.10	0.35
ANT	42.4340	-111.5930	74	4	1.60	0.28
NIT	42.4987	-111.6950	73	7	1.10	0.20
NIT	42.4987	-111.6950	73	6	1.30	0.40
NIT	42.4987	-111.6950	67	3	1.80	0.20
NIT	42.4987	-111.6950	70	10	0.90	0.20
NI2	42.4991	-111.6620	62	22	0	0
BEB	42.5201	-111.8450	49	4	1.50	0.18
BUC	42.6277	-111.8360	72	15	0	0
BUC	42.6277	-111.8360	68	6	1.00	0.10
BUC	42.6277	-111.8360	1	4	2.35	0.20

Table 1 (*continued*)

Station	Lat. (°)	Long. (°)	ϕ (°)	ϕ_{err} (°)	δt (s)	δt_{err} (s)
BA2	42.6909	-111.9190	60	19	0.30	0.15
BAN	42.6972	-111.9080	50	3	1.50	0.10
BAN	42.6972	-111.9080	77	16	1.20	0.50
BAN	42.6972	-111.9080	47	10	1.10	0.30
PEB*	42.7758	-111.9970	101	4	1.00	0.18
PEB	42.7758	-111.9970	70	4	1.25	0.12
INP	42.8457	-112.1340	34	2	2.30	0.23
MCN	42.8929	-112.2110	65	7	1.25	0.17
MCN	42.8929	-112.2110	66	4	0.80	0.10
MCN	42.8929	-112.2110	81	30	0	0
MCN	42.8929	-112.2110	81	3	1.80	0.10
MCN	42.8929	-112.2110	85	5	1.20	0.20
ANG	42.9136	-112.3240	89	12	0.70	0.17
ANG	42.9136	-112.3240	61	12	0.80	0.20
ANG	42.9136	-112.3240	68	4	1.25	0.12
ANG	42.9136	-112.3240	81	4	1.00	0.20
ANG	42.9136	-112.3240	49	6	0.95	0.18
ANG	42.9136	-112.3240	46	4	1.10	0.10
ANG	42.9136	-112.3240	57	16	0.55	0.20
ANG	42.9136	-112.3240	62	15	0	0
ANG	42.9136	-112.3240	88	7	0.90	0.20
THC	42.9618	-112.3680	78	9	1.25	0.35
THC	42.9618	-112.3680	56	10	1.15	0.20
THC	42.9618	-112.3680	65	7	1.00	0.20
FBU	42.1376	-112.5260	71	22	0	0
FBU	42.1376	-112.5260	75	4	0.95	0.10
FBU	42.1376	-112.5260	81	4	1.35	0.25
MON	43.2104	-112.6510	42	8	0.70	0.10
MON	43.2104	-112.6510	76	9	0.90	0.22
MON	43.2104	-112.6510	77	3	1.55	0.20
MON	43.2104	-112.6510	65	8	0.60	0.10
MON	43.2104	-112.6510	60	8	1.15	0.35
MON	43.2104	-112.6510	78	14	1.15	0.28
TAB	43.2869	-112.6960	59	6	1.05	0.23
TAB	43.2869	-112.6960	65	5	1.20	0.20
TAB	43.2869	-112.6960	85	10	0.60	0.20
TAB	43.2869	-112.6960	68	16	0	0
TLB	43.3791	-112.7670	45	9	1.00	0.28
TLB	43.3791	-112.7670	74	12	0.70	0.18
TLB	43.3791	-112.7670	60	5	0.90	0.15
TLB	43.3791	-112.7670	66	4	0.95	0.12
ATO	43.4259	-112.8650	57	12	1.30	0.30
ATO	43.4259	-112.8650	76	7	0	0
ILS	43.4722	-112.9220	60	7	1.80	0.40
ILS	43.4722	-112.9220	63	6	1.50	0.20
ILS	43.4722	-112.9220	79	6	1.25	0.18
ILS	43.4722	-112.9220	72	9	0	0
ILS	43.4722	-112.9220	58	6	1.35	0.18
ILS	43.4722	-112.9220	65	4	1.45	0.18
ILM	43.5417	-113.0810	67	25	0	0

Table 1 (*continued*)

Station	Lat. (°)	Long. (°)	ϕ (°)	ϕ_{err} (°)	δt (s)	δt_{err} (s)
ILM	43.5417	-113.0810	73	9	0	0
ILM	43.5417	-113.0810	67	2	1.80	0.10
ILM	43.5417	-113.0810	72	12	0	0
ILM	43.5417	-113.0810	66	3	1.40	0.12
ILN	43.6085	-113.1370	61	10	1.55	0.33
ILN	43.6085	-113.1370	63	6	1.50	0.20
ILN	43.6085	-113.1370	71	5	1.50	0.20
ARH	43.6444	-113.2190	56	2	2.00	0.18
ARH	43.6444	-113.2190	67	4	1.25	0.17
MOR	43.7050	-113.3030	69	4	1.30	0.20
MOR	43.7050	-113.3030	64	3	1.50	0.10
MOR	43.7050	-113.3030	60	2	1.75	0.12
DRL	43.7793	-113.4010	59	6	2.05	0.48
DRL	43.7793	-113.4010	60	22	0	0
DRL	43.7793	-113.4010	53	2	1.25	0.07
DRL	43.7793	-113.4010	58	5	1.10	0.15
LES	43.8451	-113.4960	67	3	1.85	0.28
LES	43.8451	-113.4960	69	2	1.75	0.18
LES	43.8451	-113.4960	51	10	1.50	0.48
LES	43.8451	-113.4960	57	14	0	0
LES	43.8451	-113.4960	70	25	0	0
LES	43.8451	-113.4960	58	14	1.15	0.35
MAC	43.9265	-113.5300	71	30	0	0
MAC	43.9265	-113.5300	64	5	1.35	0.27
MCR	43.9940	-113.6340	40	9	1.30	0.20
MCR	43.9940	-113.6340	61	5	1.75	0.30
MCR	43.9940	-113.6340	56	4	1.65	0.17
MCR	43.9940	-113.6340	47	5	1.80	0.18
MCR	43.9940	-113.6340	62	4	1.20	0.20
MCR	43.9940	-113.6340	60	14	0	0
LCC	44.0366	-113.7510	61	2	1.50	0.15
LCC	44.0366	-113.7510	62	14	0	0
LCC	44.0366	-113.7510	60	3	1.35	0.15
LCC	44.0366	-113.7510	69	9	0.80	0.10
LCC	44.0366	-113.7510	82	2	1.30	0.10
LCC	44.0366	-113.7510	78	16	0.75	0.25
LCC	44.0366	-113.7510	62	2	1.80	0.12
BOR	44.1266	-113.8370	74	6	1.50	0.20
BOR	44.1266	-113.8370	53	10	1.25	0.25
DKP	44.2220	-113.9460	68	4	1.40	0.23
DKP	44.2220	-113.9460	50	10	1.20	0.30
DKP	44.2220	-113.9460	62	8	1.00	0.22
DKP	44.2220	-113.9460	63	4	1.30	0.15
BWC	44.2556	-114.0200	72	15	0	0
BWC	44.2556	-114.0200	73	4	1.35	0.15
BWC	44.2556	-114.0200	57	10	1.40	0.30
SPC	44.3146	-114.1060	80	4	0.95	0.20
SPC	44.3146	-114.1060	66	8	0	0
LPP	44.3736	-114.1930	1	4	2.60	0.33
LPP	44.3736	-114.1930	84	5	1.60	0.20

Table 1 (*continued*)

Station	Lat. (°)	Long. (°)	ϕ (°)	ϕ_{err} (°)	δt (s)	δt_{err} (s)
LPP	44.3736	-114.1930	69	15	0	0
BIC	44.4372	-114.2340	71	5	1.10	0.23
BIC	44.4372	-114.2340	80	7	1.10	0.20
BIC	44.4372	-114.2340	63	12	0.80	0.30
BIC	44.4372	-114.2340	58	9	0.70	0.10
DSP	44.4949	-114.3330	81	5	1.00	0.10
DSP	44.4949	-114.3330	79	7	1.30	0.20
DSP	44.4949	-114.3330	48	7	1.40	0.20
DSP	44.4949	-114.3330	90	10	0	0
DSP	44.4949	-114.3330	40	20	0.60	0.27
MQR*	44.5490	-114.4020	83	4	4.00	0.05
TWP	44.6031	-114.4720	75	2	1.45	0.18
TWP	44.6031	-114.4720	62	14	0	0
TWP	44.6031	-114.4720	82	10	0	0
TWP	44.6031	-114.4720	54	22	0.55	0.25
TWP	44.6031	-114.4720	83	8	0.95	0.20
TWP	44.6031	-114.4720	76	17	1.00	0.40
TWP	44.6031	-114.4720	76	3	1.40	0.10
SDM	44.7622	-114.6660	71	22	0.45	0.18
SDM	44.7622	-114.6660	71	9	0.90	0.20
SDM	44.7622	-114.6660	85	6	1.20	0.20

Raw splitting data: all measurements with $\delta t \leq 0.5$. ϕ_{err} and δt_{err} are 95% confidence bounds. A δt of 0 indicates a null split. Based on transverse energy patterns, we believe four of our split estimates are incorrect. These are marked with an asterisk.

Results

Results are tabulated in Table 1 and shown in Figure 4. Thin lines in this figure indicate the orientation and split time of the measured split; thick lines indicate the back azimuth of the null splits (their lengths have been scaled to 1.0 s). Fast axis orientations are nearly constant across the array, with little dependence on station location or back azimuth. The angle histogram in Figure 4 emphasizes the narrow range in fast axis orientation of about 30°.

The relative consistency in splitting parameters with back azimuth allows us to discount Core Mantle Boundary (CMB) splitting as a source of the observed SKS splits (because CMB splitting would produce split parameters that vary with back azimuth) and to conclude that there is no general trend of strongly dipping fast axes across our array (also suggested by the absence of variation in split parameters with back azimuth, Fig. 5, SILVER and SAVAGE, 1994). This latter observation leads us to make the considered assumption that the fast axis is transverse in the eSRP.

The null splits, in addition to constraining the fast axis orientation into one of four orientation bands (Fig. 3—Bottom), offer important information on the simplicity of the anisotropy orientation structure. If orientation structure varies

with depth, null splits would not occur (except in the case of layers of orthogonally oriented anisotropy). Thus the null splits indicate that the mantle beneath the eSRP is comprised of a single layer of transversely anisotropic material.

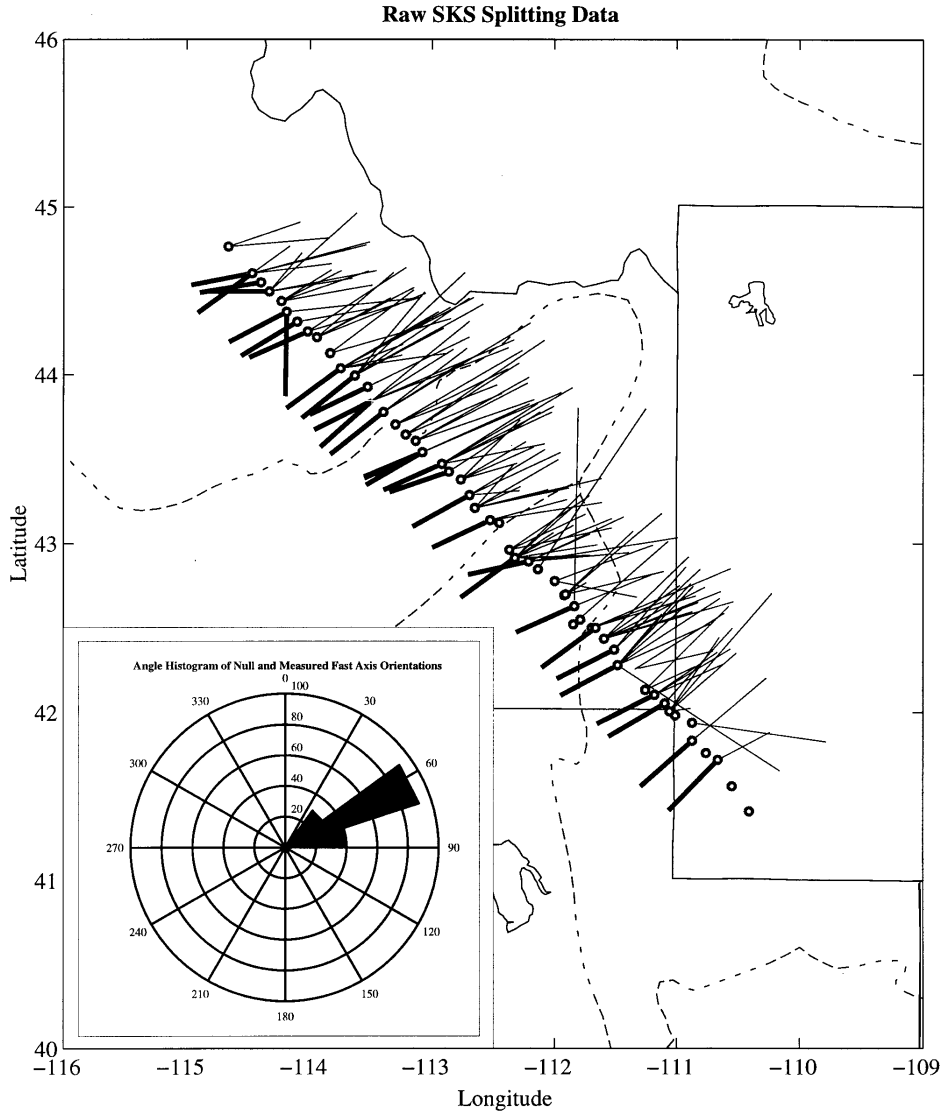


Figure 4

Raw-splitting results. Measured splits are shown with thin lines extending to the northeast, and nulls are shown with thick lines extending to the southwest. Line orientation shows the fast-axis orientation, and line length is proportional to the split time (which ranges from 0.5–1.5 s); null lengths have been set to a split time of 1 s. Both null and split measurements are limited to an azimuth of $0 < \phi < 180$. Inset is an angle histogram of measured and null orientations.

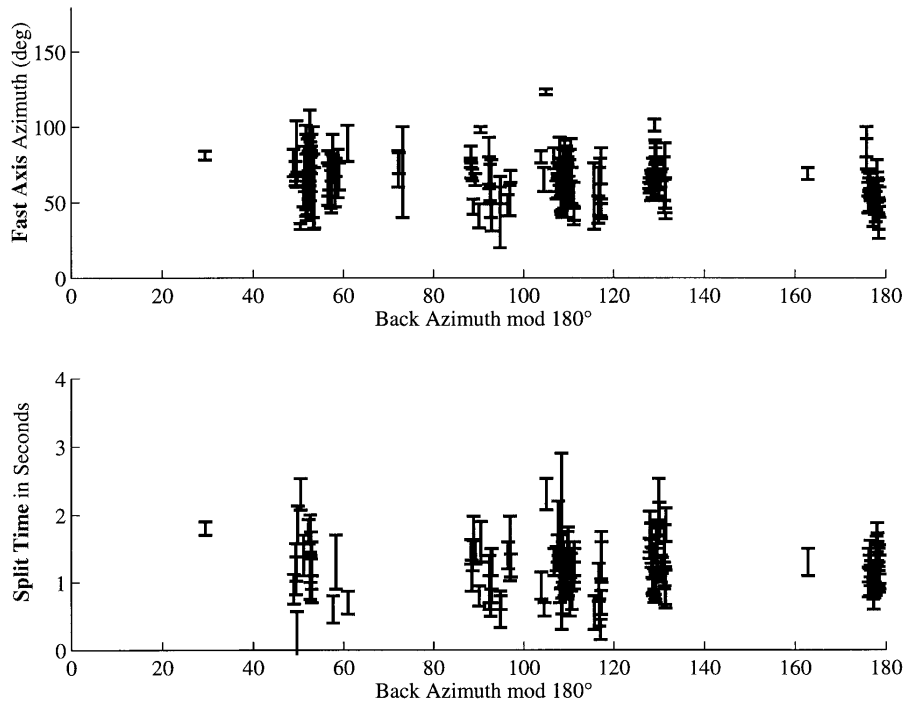


Figure 5

Split parameters with event back azimuth mod 180, using data from Table 1 ($\delta t_{\text{err}} < 0.5$ s). We have excluded the event with $\delta t = 4.0$ s. Error bars show the calculated 95% confidence intervals. We see no trend with back azimuth, suggesting that splitting occurs near our array. Actual distribution of back azimuths is void of events with back azimuths from the southeast hemisphere.

Four of our split measurements (of 171) are inconsistent with the other observations. These split determinations have transverse energy plots that appear unusual and whose results are inconsistent with our other estimates. They have still been included in our analysis, and turn out to have no significant effect on our findings.

Station Average

The independence of split parameters with back azimuth implies that anisotropy is essentially homogeneous under each station. When this is the case, it then is valid to average splitting parameters by station. SILVER and CHAN (1991) use F test statistics to determine the uncertainty estimates of split parameters. We extend this technique to station averages, which allows us to incorporate both null and observed splits into our estimates (Fig. 6 and Table 2).

Figure 7 shows station averaged split parameters. Split time averages vary from 0.5–1.5 s across the array, implying significant changes in either anisotropy magnitude or layer thickness across the array. In contrast, the orientations are quite uniform, although the northernmost stations differ in orientation by a small but resolvable amount (Fig. 8).

Discussion

By considering the trade-off between path length through anisotropic material and degree of anisotropy, we conclude that at least some of the observed anisotropy resides in the asthenosphere. For instance, an average anisotropy magnitude of 4% and a split time of 1.25 s implies a path length of nearly 150 km (Fig. 9). Using receiver functions, PENG and HUMPHREYS (1997) find the crust to be about 40 km thick and not strongly anisotropic. Unless the lithospheric mantle is 110 km thick

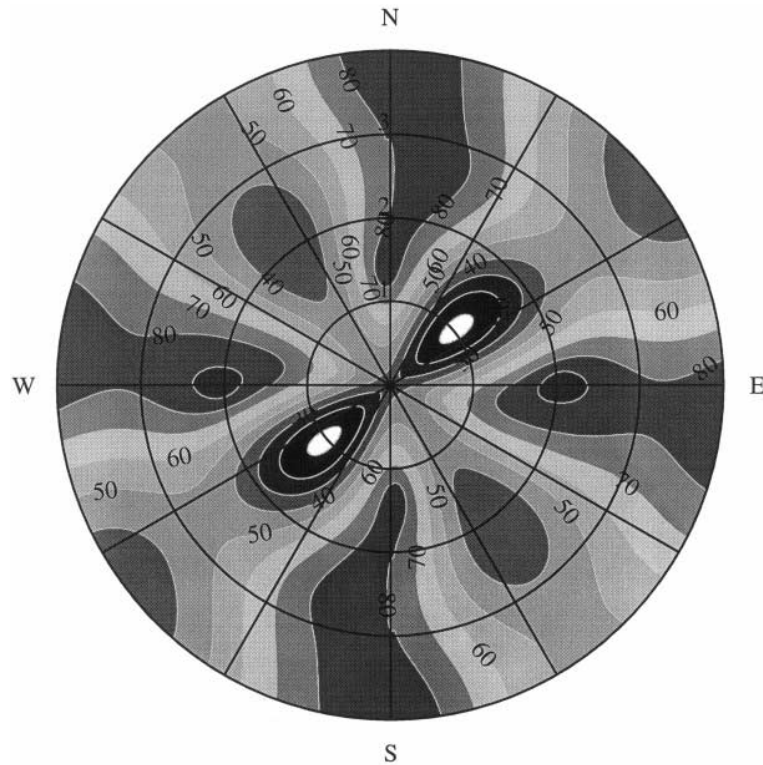


Figure 6

Plot of summed transverse energy for a selected station. Both split and null-split energies contribute to this sum. Four separate split measurements were combined to make this plot. Energy amplitude is arbitrary; an F test is applied to this sum to convert summed energy to probability at each point. The white region is an area of greatest likelihood, and represents roughly 95% confidence bounds.

Table 2
Station averaged splitting data

Station	Lat. (°)	Long. (°)	ϕ (°)	ϕ_{err} (°)	δt (s)	δt_{err} (s)	# of files used
CAR	41.4100	-110.4100	-70	-20 +18	2.1	-0.8 +1.0	2
HOG	41.5600	-110.5500	-56	-61 +60	1.4	-2.0 +2.0	1
CAV	41.7170	-110.6650	53	-61 +60	0.6	-1.0 +2.0	2
FOS	41.7579	-110.7600	-47	-61 +60	0.3	-0.3 +0.6	10
NUG	41.8311	-110.8740	57	-7 +07	4.0	-2.0 +2.0	1
NU2	41.8319	-110.8740	50	-20 +16	1.0	-0.4 +0.5	2
LDC	41.9375	-110.8730	10	-36 +60	0.4	-0.4 +1.1	2
CHC	41.9811	-111.0110	79	-25 +25	4.0	-2.0 +1.8	1
CH2	42.0058	-111.0570	47	-7 +07	1.1	-0.2 +0.2	4
DAH	42.0522	-111.0960	67	-22 +19	2.2	-2.0 +2.0	3
VOS	42.1030	-111.1800	58	-9 +09	0.9	-0.3 +0.3	4
MEM	42.1317	-111.2560	41	-13 +14	1.3	-0.4 +0.3	2
AIR	42.2541	-111.3390	69	-19 +28	1.1	-0.5 +0.5	2
MIC	42.2784	-111.4820	53	-13 +13	1.0	-0.4 +0.3	8
EMC	42.3694	-111.5090	52	-10 +09	0.7	-0.6 +0.6	2
ANT	42.4340	-111.5930	64	-7 +06	1.3	-0.3 +0.2	8
NIT	42.4987	-111.6950	64	-19 +19	0.9	-0.7 +0.7	2
NI2	42.4991	-111.6620	62	-13 +13	1.3	-1.5 +2.0	1
BEB	42.5201	-111.8450	49	-14 +13	1.5	-0.4 +0.4	1
BCN	42.5473	-111.7880	65	-20 +36	0.9	-0.6 +0.6	2
BUC	42.6277	-111.8360	-90	-61 +34	0.5	-0.5 +0.8	6
BA2	42.6909	-111.9190	60	-18 +40	0.3	-0.1 +0.1	1
BAN	42.6972	-111.9080	53	-20 +18	1.2	-0.4 +0.5	3
PEB	42.7758	-111.9970	71	-16 +13	1.2	-0.3 +0.2	2
INP	42.8457	-112.1340	34	-8 +06	2.3	-0.7 +0.9	1
MCN	42.8929	-112.2110	66	-14 +16	0.9	-0.3 +0.3	5
ANG	42.9136	-112.3240	66	-18 +21	0.8	-0.4 +0.3	11
THC	42.9618	-112.3680	70	-17 +17	1.0	-0.4 +0.4	4
FBU	43.1376	-112.5260	-88	-35 +38	0.7	-0.4 +0.5	4
MON	43.2104	-112.6510	71	-16 +13	0.8	-0.2 +0.4	7
TAB	43.2869	-112.6960	70	-18 +38	0.8	-0.5 +0.4	4
TLB	43.3791	-112.7670	55	-15 +14	0.8	-0.3 +0.2	3
ATO	43.4259	-112.8650	-47	-61 +60	0.2	-0.2 +0.4	2
ILS	43.4722	-112.9220	70	-10 +10	1.3	-0.4 +0.3	4
ILM	43.5417	-113.0810	67	-6 +05	1.6	-0.3 +0.2	7
ILN	43.6085	-113.1370	61	-20 +21	1.6	-0.7 +0.7	1
ARH	43.6444	-113.2190	60	-9 +07	1.6	-0.5 +0.6	3
MOR	43.7050	-113.3030	60	-7 +06	1.7	-0.3 +0.3	3
DRL	43.7793	-113.4010	57	-10 +08	1.1	-0.2 +0.3	5
LES	43.8451	-113.4960	65	-8 +07	1.7	-0.5 +0.5	8
MAC	43.9265	-113.5300	65	-13 +11	1.5	-0.7 +0.7	3
MCR	43.9940	-113.6340	60	-9 +08	1.5	-0.4 +0.3	6
LCC	44.0366	-113.7510	63	-8 +07	1.5	-0.4 +0.3	7
BOR	44.1266	-113.8370	64	-15 +13	1.5	-0.6 +0.6	3
DKP	44.2220	-113.9460	66	-12 +10	1.3	-0.4 +0.3	3
BWC	44.2556	-114.0200	66	-9 +09	1.2	-0.6 +0.6	5
SPC	44.3146	-114.1060	72	-16 +15	0.9	-0.6 +0.5	2
LPP	44.3736	-114.1930	75	-14 +14	1.3	-0.6 +0.7	4
BIC	44.4372	-114.2340	72	-12 +10	1.0	-0.3 +0.3	3

Table 2 (*continued*)

Station	Lat. (°)	Long. (°)	ϕ (°)	ϕ_{err} (°)	δt (s)	δt_{err} (s)	# of files used
DSP	44.4949	-114.3330	78	-14 +13	0.9	-0.5 +0.4	5
MQR	44.5490	-114.4020	83	-61 +60	4.0	-2.0 +2.0	1
TWP	44.6031	-114.4720	77	-12 +11	0.9	-0.4 +0.4	6
SDM	44.7622	-114.6660	78	-49 +21	0.7	-0.5 +0.5	2

Station averaged splitting data. Using the principle that the sum of χ^2 variables is itself a χ^2 variable, and following the assumption of SILVER and CHAN (1991) that the transverse energy is nearly a χ^2 variable; we sum corrected transverse energies $E_t(\phi, \delta t)$ by station. ϕ_{err} and δt_{err} are rough 95% confidence bounds. # of files used column indicates number of corrected transverse energy files (split measurements) summed to obtain the station average. We note that this technique allows us to incorporate more poorly constrained measurements than in Table 1, hence the data in Tables 1 and 2 are not 1-1. In general the data in Table 1 are a subset of the data used to make Table 2, except for six misplaced files which are in Table 1 but not in Table 2.

or more—a huge amount given that the array is situated off the craton, in a hot and extensional environment—some of the anisotropy measured (and likely most of it) must be caused by anisotropic asthenosphere.

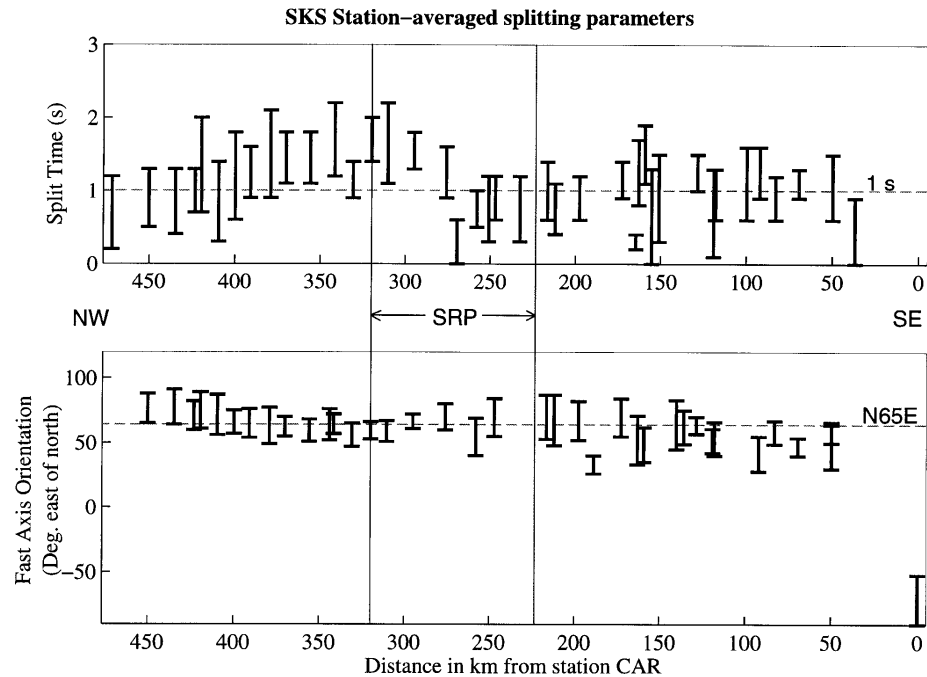


Figure 7

Station-averaged splitting results, obtained from the F -test results derived from plots exemplified by Figure 5. A depression in split time is seen, centered southeast of the axis of the Snake River Plain (SRP). Results with major errors have not been plotted: total $\delta t_{\text{err}} > 1.4$ s or total $\phi_{\text{err}} > 40^\circ$ (all results tabulated in Table 2).

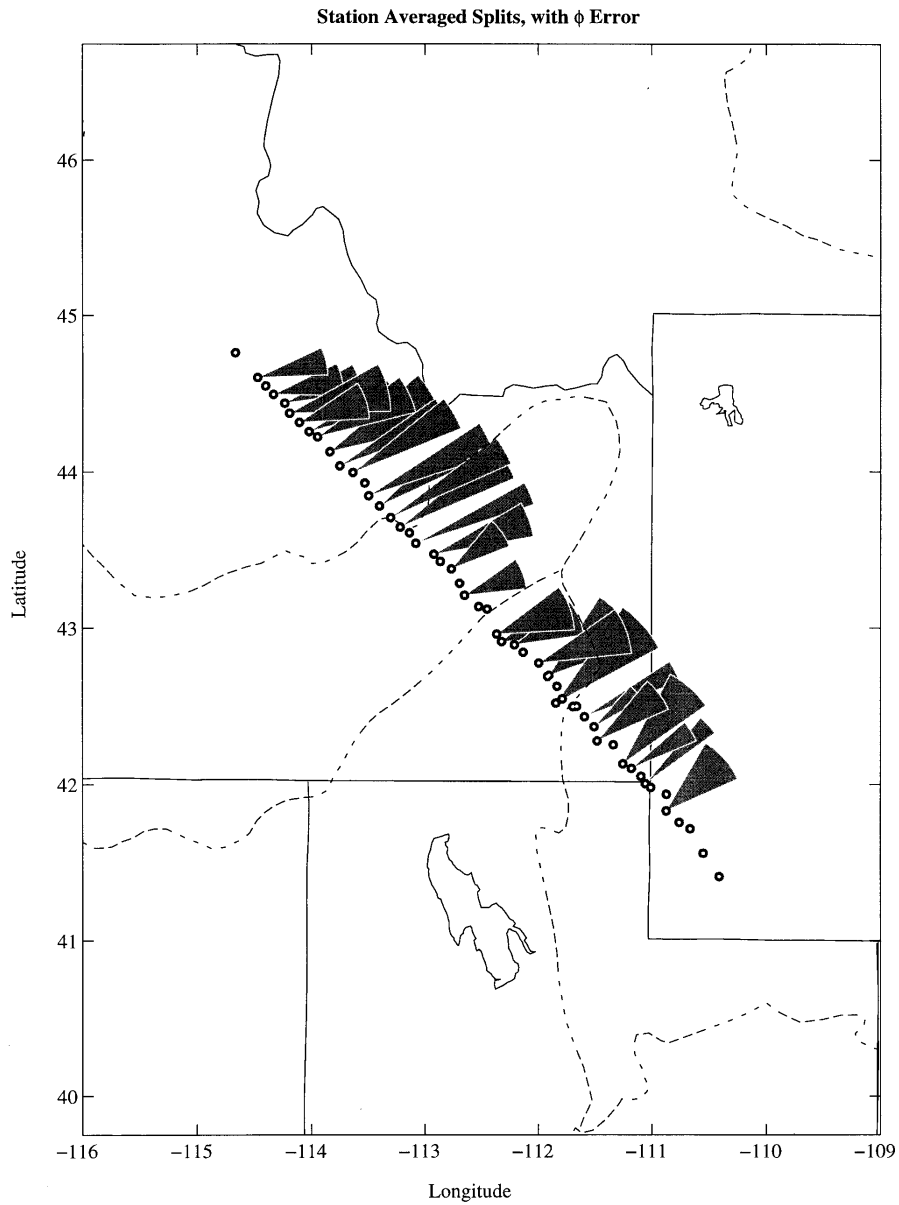


Figure 8

Station-averaged splits plotted in a map view. Width of each sector indicates approximate 95% confidence bounds in orientation of the fast axis. Split times range from 0.3–1.5 s (confidence bounds are not shown for clarity). Station averages with total $\delta t_{\text{err}} > 1.4$ s or $\phi_{\text{err}} > 40^\circ$ are not shown. Fast axis orientations to stations in the northwest appear to be systematically rotated with respect to the other stations.

It might be expected that the complex deformation history of this area would result in a complicated lithospheric (fossil) anisotropy structure. Shear-wave splitting measurements in Colorado exhibit a very complex structure, including a wide variety of null orientations. Splitting measurements in Nevada, although simpler, have neither the degree of uniformity nor the orientation of the eSRP splits (Fig. 10). Since most (and perhaps all) of our anisotropy resides in the asthenosphere, the Lattice Preferred Orientation (LPO) inducing flow under the eSRP is thought to postdate the Laramide orogeny (when the subducted slab is thought to have passed beneath this region at a depth of ~ 100 km depth (HUMPHREYS and DUEKER, 1994)). Because anisotropy tends to align with the most recent significant strain event (RIBE, 1992), we conclude that hot spot activity and absolute plate motion are responsible for the observed anisotropy field, and that any previously existing

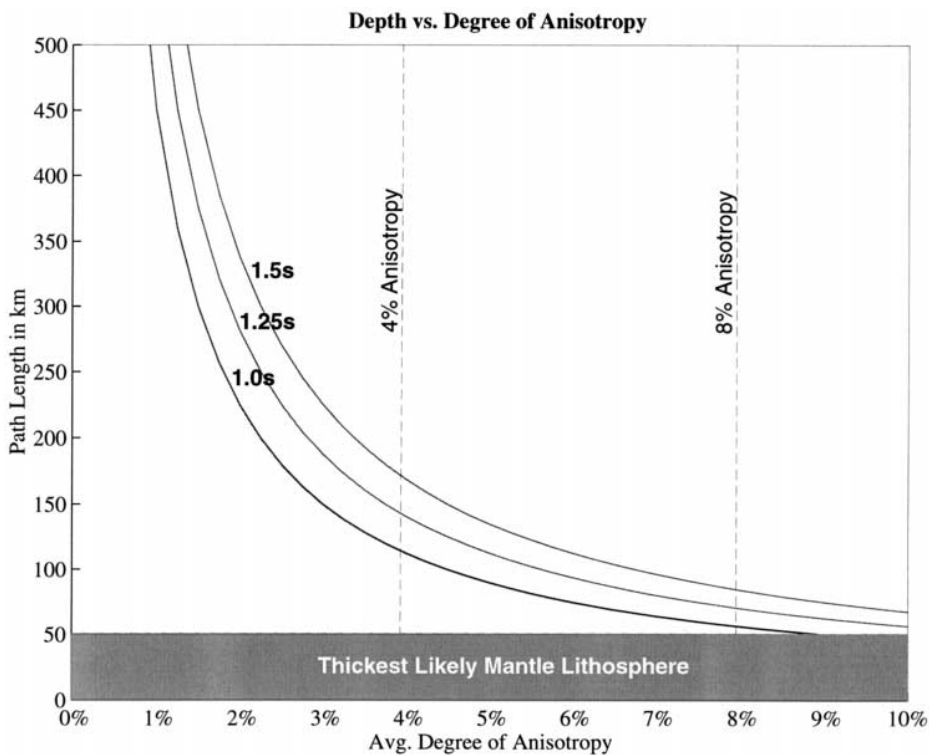


Figure 9

Plot of trade-off between path length L , anisotropy magnitude $\delta\beta$, path-averaged anisotropy magnitude $\delta\hat{\beta}_0$, and split time δt , using the relation $L = \beta_0 \delta t / \delta\hat{\beta}_0$, where β_0 is the average of fast and slow axes shear velocities (taken to be 4.5 km/s). Given an anisotropy magnitude of 4% and a split time of 1.25 s, this relation implies a path length of nearly 150 km. The 40 km thick crust is only weakly anisotropic (PENG and HUMPHREYS, 1997). As it is highly unlikely that the lithospheric mantle is 110 km thick or more, some, and probably most, of the anisotropy must lie in the asthenosphere.

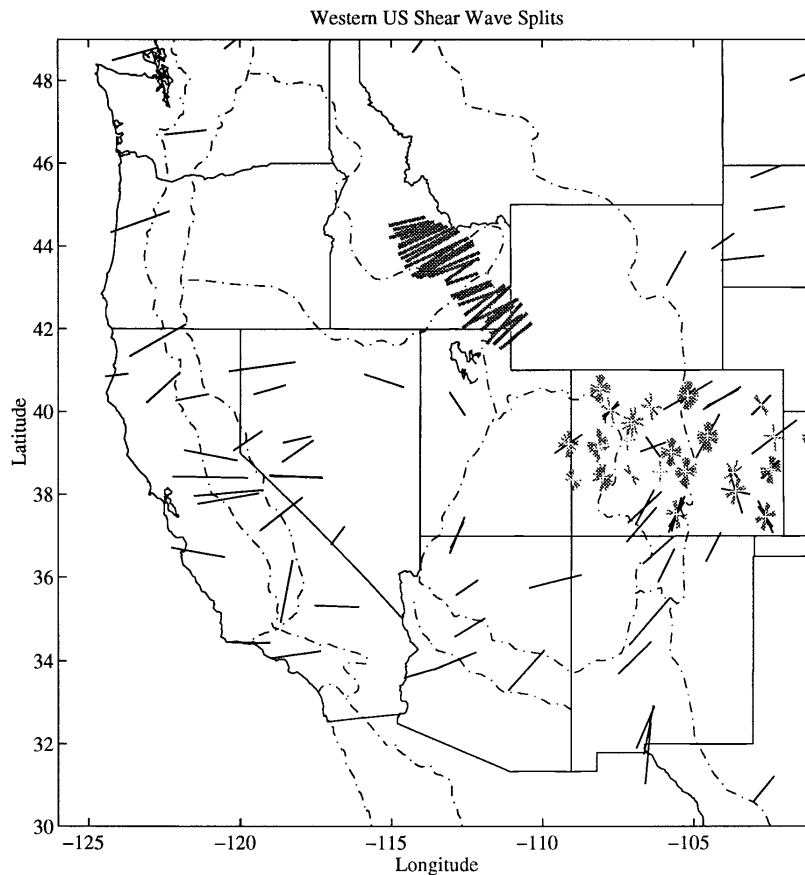


Figure 10

Eastern Snake River Plain station-averaged splits shown in regional context. Eastern Snake River Plain splits are plotted as thick dark gray lines; other measured splits are shown with thin, solid lines; and null splits (only in Colorado and Kansas) are plotted as short light gray lines. [Split data from BOSTOCK and CASSIDY, 1995; SANDVOL *et al.*, 1992; VINNIK *et al.*, 1992; SILVER and CHAN, 1991; HELFFRICH *et al.*, 1994; SILVER and KANESHIMA, 1993; RUPPERT, 1992; BARRUOL *et al.*, 1996; OZALAYBEY and SAVAGE, 1995; SAVAGE *et al.*, 1996].

anisotropy has been reset or erased. If so, the uniform orientation structure found beneath our array lies within the asthenospheric wake of the hot spot. This is consistent with the asthenospheric wake inferred by surface deformation and uplift, but since our array does not extend beyond the tectonic parabola, the width of our investigation suggests only a minimum width of the asthenospheric wake.

The anisotropy and velocity structures provide an interesting contrast (Fig. 11). Anisotropy orientation is rather uniform across the array, whereas the *S*-wave velocity structure is very heterogeneous. SALTZER and HUMPHREYS (1997) argue

that the P -wave velocity structure—which is very similar to the S -velocity structure—is produced largely by variations in partial melt content. If so, the melt distribution is independent of the anisotropy orientation field.

The measured anisotropy, which is thought to indicate the strain state of the anisotropic material, can provide useful information on the dynamic behavior of the asthenosphere. The two mechanisms thought to be most important in creating asthenospheric strain in this region are North American absolute plate motion (a passive mechanism) and flattening of anomalously buoyant mantle (a self-driven, or active mechanism). These mechanisms can be distinguished from each other by the orientation of the anisotropy they would produce. North American absolute plate motion would excite a simple shear flow field that orients the anisotropic fast axis parallel to the eSRP axis, whereas buoyancy-driven flattening would drive pure shear deformation (vertical shortening and extension approximately normal to the eSRP) with the fast axis oriented normal to the eSRP. The fast-axis orientation is nearly parallel to the eSRP axis, consistent with being aligned primarily by North American plate motion. In detail, the fast-axis orientation appears to rotate from about N80E at the northernmost stations to about N60E near the middle of the array (Absolute Plate Motion of the eSRP is $N60 \pm 20^\circ E$ (GRIPP and GORDON, 1990); the most recent trend of rhyolitic volcanism is $N54 \pm 5^\circ E$ (PIERCE and

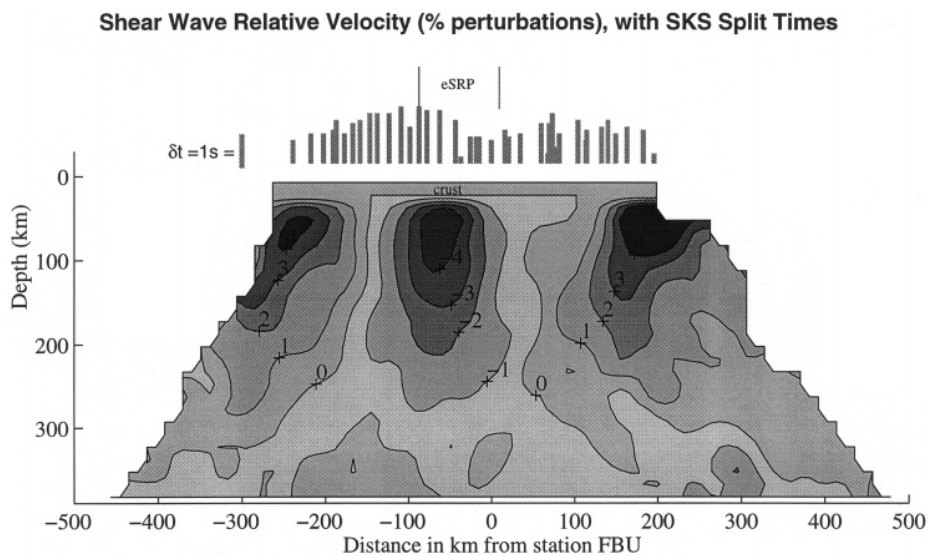


Figure 11

Upper mantle shear-wave velocity and station-averaged split times. (Split times with $\delta t_{\text{err}} > 1.4$ s are not shown). The depression in split times appears not to correlate with velocity structure. However, because all split determinations are derived from arrivals emanating from the NW, it is possible that the offset pattern is a result of being projected to the SE.

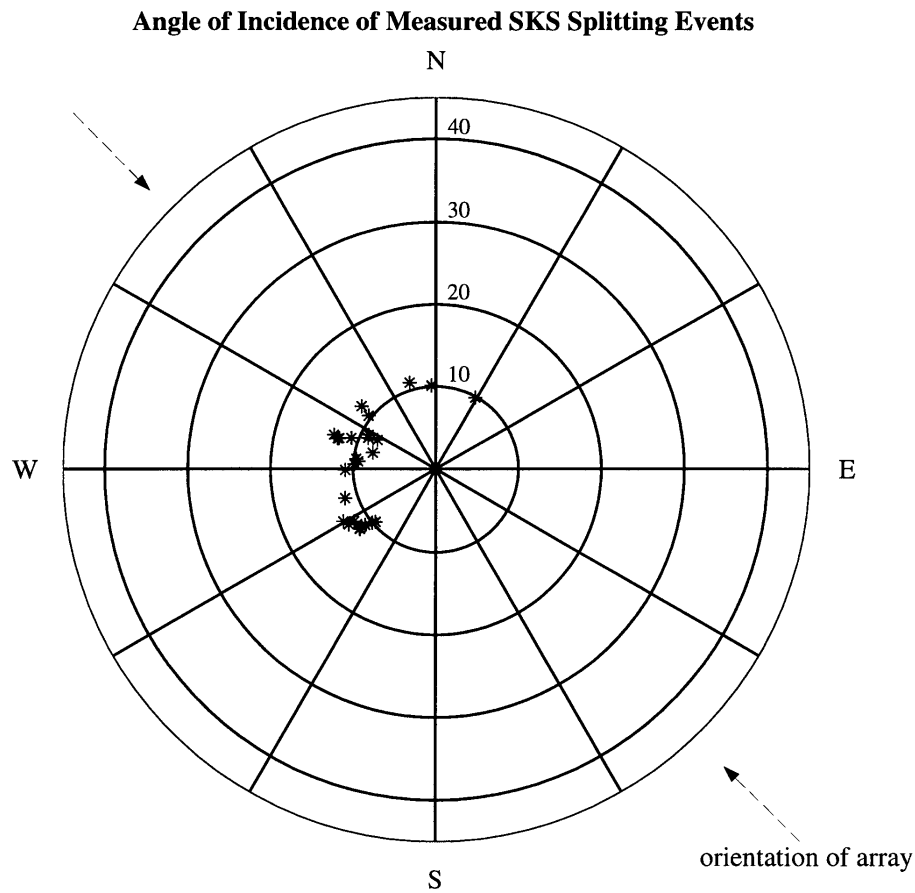


Figure 12
SKS splitting events plotted by back azimuth and angle of incidence.

MORGAN, 1992)). This trend may indicate a flattening-produced component to the integrated strain field producing the anisotropy.

Split time structure has a significant depression in station-averaged split times near the center of the array. This depression is centered about 60 km southeast of the eSRP (near the southern boundary of the eSRP). Because none of our SKS rays arrive from the southeast, the station averages are most likely projections of structure to the northwest (Fig. 12). If the anisotropy responsible for the splits were located at a depth of $\sim 200\text{--}300$ km it would be centered beneath the eSRP. The cause of the reduced anisotropy is not known. Candidate solutions include the presence of melt films oriented so as to partially compensate for the LPO, and reduced horizontal LPO development (perhaps because of upward flow or an LPO-inhibiting influence of partial melt).

REFERENCES

- ANDERS, M. H., and SLEEP, N. M. (1992), *Lithospheric Strengthening by Magmatic Intrusion, Thermal and Mechanical Effects of the Yellowstone Hotspot*, J. Geophys. Res. 97, 15,379–15,394.
- BARRUOL, G., SILVER, P. G., and VAUCHEZ, A. (1996), *Seismic Anisotropy in the Eastern United States: Deep Structure of a Complex Continental Plate*, J. Geophys. Res. 102, 8329–8348.
- BOSTOCK, M. G., and CASSIDY, J. F. (1995), *Variations in SKS Splitting Across the Canadian National Seismic Network*, Geophys. Res. Lett. 22, 5–8.
- GRIFF, A. E., and GORDON, R. G. (1990), *Current Plate Velocities Relative to the Hotspots Incorporating the NUVEL-1 Global Plate Motion Model*, Geophys. Res. Lett. 17, 1109–1112.
- HEARN, E. H., KENNEDY, B. M., and TREUSDELL, A. H. (1990), *Coupled Variations in Helium Isotopes and Fluid Chemistry: Shoshone Geyser Basin, Yellowstone*, Geochimica et Cosmochimica Acta 54, 3103–3113.
- HELFFRICH, G., SILVER, P. G., and GIVEN, H. (1994), *Shear-wave Splitting Variation over Short Spatial Scales on Continents*, Geophys. J. Int. 119, 561–573.
- HUMPHREYS, E. D., and DUEKER, K. G. (1994), *Physical State of the Western US Upper Mantle*, J. Geophys. Res. 99, 9635–9650.
- MILBERT, D. G. (1991), *GEOID90: A High-resolution Geoid for the United States*, EOS, Trans. Am. Geophys. Union 72, 49.
- OZALAYBEY, S., and SAVAGE, M. K. (1995), *Shear-wave Splitting beneath Western United States in Relation to Plate Tectonics*, J. Geophys. Res. 100, 18,135–18,149.
- PENG, X., and HUMPHREYS, E. (1997), *Crustal Velocity Structure of the Eastern Snake River Plain*, J. Geophys. Res., in press.
- PIERCE, K. L., and MORGAN, L. A. (1992), *The Track of the Yellowstone Hot Spot: Volcanism, Faulting, and Uplift*, Memoir-Geological Soc. Am. 179, 1–53.
- RIBE, N. M. (1992), *On the Relation between Seismic Anisotropy and Finite Strain*, J. Geophys. Res. 97, 8737–8747.
- RIBE, N. M., and CHRISTENSEN, U. (1994), *Dynamical Modeling of Plume-lithosphere Interaction*, J. Geophys. Res. 99, 669–682.
- RUPPERT, S. (1992), *Tectonics of Western North America: A Teleseismic View*, Ph.D. Thesis, Stanford Univ., 216 pp.
- SALTZER, R., and HUMPHREYS, E. (1997), *Upper Mantle P-wave Velocity Structure of the Eastern Snake River Plain and its Relationship to Geodynamics Models of the Region*, J. Geophys. Res. 102, 11829–11842.
- SANDVOL, E., NI, J., OZALAYBEY, S., and SCHUE, J. (1992), *Shear-wave Splitting in the Rio Grande Rift*, Geophys. Res. Lett. 2 19, 2337–2340.
- SAVAGE, M. K., SHEEHAN, A. F., and LERNER-LAM, A. (1996), *Shear-wave Splitting across the Rocky Mountain Front*, Geophys. Res. Lett. 23, 2267–2270.
- SILVER, P. G., and CHAN, W. W. (1991), *Shear-wave Splitting and Subcontinental Mantle Deformation*, J. Geophys. Res. 96, 16429–16454.
- SILVER, P. G., and KANESHIMA, S. (1993), *Constraints on Mantle Anisotropy beneath Precambrian North America from a Transportable Teleseismic Experiment*, Geophys. Res. Lett. 20, 1127–1130.
- SILVER, P. G., and SAVAGE, M. K. (1994), *The Interpretation of Shear-wave Splitting Parameters in the Presence of Two Anisotropic Layers*, Geophys. J. Int. 119, 949–963.
- SMITH, R. B., and BRAILE, L. W. (1994), *The Yellowstone Hotspot*, J. Volc. Geotherm. Res. 61, 121–188.
- SPARLIN, M. A., BRAILE, L. W., and SMITH, R. B. (1982), *Crustal Structure of the Eastern Snake River Plain Determined from Ray Trace Modeling of Seismic Refraction Data (Idaho)*, J. Geophys. Res. 87, 2619–2633.
- VINNIK, L. P., MAKEYEVA, L. I., MILEV, A., and USENKO, Y. (1992), *Global Patterns of Azimuthal Anisotropy and Deformation in the Continental Mantle*, Geophys. J. Int. 111, 433–447.

(Received October 14, 1996, revised April 29, 1997, accepted June 18, 1997)